Chapter 16
High-frequency Dynamic Characterization of Rubber Mounts through an Enhanced Virtual Point Transformation

Bart Forrier, Fabio Bianciardi, and Karl Janssens

Abstract Rubber mounts are critical components in the optimization of vehicle designs towards noise, vibration and harshness performance. In virtual prototyping applications, they are often represented by experimentally identified dynamic stiffness curves. The latter are extracted, partly via inverse substructuring or decoupling, from frequency response function measurements. Dedicated fixtures are hereby instrumental: excitation and response measurements are distributed over the fixture. Afterward, the so-called virtual point transformation condenses them into six degrees of freedom at one central point on each side of the mount, under the assumption that the fixtures behave rigidly. As the frequency range of interest reaches up to or beyond the first natural frequencies of the fixtures, though, the dynamics of the fixtures pollute the identified mount stiffness curves. Therefore, this work aims to increase the accuracy of rubber mount characterizations toward high frequencies through an enhanced virtual point transformation. This enhanced transformation considers fixture deformation, though it finally preserves the condensation into six degrees of freedom per side. The latter feature is critical for smoothly integrating the experimental mount model into various virtual prototype assemblies. Through a numerical validation, this work shows, firstly, that finite element model based natural mode shapes of the fixture form a well-suited basis for capturing its deformation. A subsequent experimental validation deals with the characterization of an actual automotive rubber mount, accounting for one flexible mode of the fixture assembly. The results demonstrate that the proposed enhancement indeed extends the useful identification bandwidth, to beyond the first natural frequency introduced by the fixture assembly.

Keywords Mount stiffness · High-Frequency · Experimental · Dynamic substructuring

Introduction

Noise, vibration, and harshness (NVH) performance is an important differentiator in today's automotive vehicle market. Whilst customer expectations increase continuously, engineering efforts and costs must kept as low as possible. In relation to NVH engineering, the field of virtual acoustic prototyping has emerged to tackle those conflicting requirements [1]. Nowadays, virtual prototype assembly (VPA) technology supports NVH engineers with predictive NVH performance analyses [2]. This technology is based on component-based transfer path analysis (C-TPA) methods [3]. Dynamic substructuring (DS) is hereby employed to determine the structural-vibration characteristics of an assembly from those of its constituent components [4, 5].

The advent of hybrid and battery electric vehicles (BEV) has brought additional NVH challenges, in large part originating from the enlarged frequency bandwidth over which an electric motor excites both acoustic and structural noise transfer paths [2]. Accordingly, post-factum or predictive TPA are now required to be accurate up to several kHz, also for what regards the structure-borne paths. Because these paths often include rubber mounts, the latter's vibration characteristics must be known accurately over an ever larger frequency bandwidth – exceeding those attainable using standard practice [6].

In a VPA framework, inter-component connections are represented as point connections with a maximum of 6 degrees of freedom (DOF), Therefore, a complete mount characterization relates applied forces and moments to vibration responses using 6 degrees of freedom (DOF) on each side, Several methods exist to determine such twelve DOF mount models experimentally [7]. They rely on the so-called virtual point transformation (VPT) to project a set of measured non-collocated frequency response functions (FRF) onto the six DOF associated with one connection point [8]. In practice, a fixture (often cross-shaped and made out of steel or aluminium) is attached to each side of the mount. The role of the fixture is to

Bart Forrier · Fabio Bianciardi · Karl Janssens
RTD Department of Test and Smart Vehicle Technology, Siemens Digital Industries Software NV, Leuven, Belgium
e-mail: bart.forrier@siemens.com; fabio.bianciardi@siemens.com; karl.janssens@siemens.com

Walter D'Ambrogio, et al. (eds.), *Dynamic Substructuring & Transfer Path Analysis, Vol. 4*, Conference Proceedings of the Society for Experimental Mechanics Series, https://doi.org/10.13052/97887-438-0149-8_16

facilitate excitation and response measurements, ensuring proper excitation and observation of all six DOF [7]. The addition of such fixtures does not change the obtained dynamic transfer stiffness of the mount [9]. The full dynamic stiffness matrix of only the mount can also be obtained, via the so-called round-trip identity method [9, 10], inverse substructuring [10, 7] or structural decoupling through frequency based substructuring (FBS)[7].

The aforementioned methods yield accurate dynamic characterizations at frequencies up to about 1 kHz. As the frequency range of interest reaches into the multi-kHz range, though, the fixtures start to behave as flexible components [7]. This violates the assumption of rigidity which is at the heart of the VPT [8]. Making a fixture more rigid, though, would yield additional drawbacks related to the addition of mass. Firstly, it attenuates the vibration response at higher frequencies, which leads to noisy FRF measurements [9]. Secondly, obtaining the point-wise dynamic mount stiffness values requires one to subtract the effect of the crosses from the measured assembly stiffness. The latter decoupling problem is ill-conditioned for a combination of higher frequencies and/or larger mass values, leading to amplification of phase measurement errors [7].

In the context of FBS, extensions to VPT have been proposed in order to relax on the requirement of local rigidity around the connection points [11, 12]. In essence, this is done by extending the original set of 6 rigid interface displacement modes with additional interface deformation modes (IDM). Depending on the application case, a limited set of pre-defined IDM may be cherry-picked from a library of general deformation modes [11]. Alternatively, the expected strain field around the interface may motivate one to assume local beam- or plate-like behavior. In such case, the corresponding IDM can be obtained by fitting polynomial beam or plate deformation models onto the measured data [12]. These extensions have targeted FBS applications where matching additional flexible DOF are introduced to both components to be coupled.

The addition of extra DOF is not feasible when using VPA for design optimization, however. As different component models may originate from different teams or vendors, the inclusion of the same amount of flexible DOF on either side would likely still result in incompatible interface deformation representations. Moreover, the entire library of variants or replacement components should be made compatible with the extra DOF introduced in one adjacent component, which is not at all feasible. Keeping in mind the VPA application, this work therefore proposes to complement the extension of the VPT with flexible DOF, with a subsequent reduction to maintain six DOF per connection point. We propose to extend the VPT with normal modes obtained from a finite element model (FEM) of the fixtures. The FEM based shapes can be accurate yet obtained with relative ease, thanks to the simple geometry and monolithic nature of typical fixtures. The subsequent reduction to six DOF, though not advisable in the general context of DS, will prove to be well-suited for the purpose of mount characterization.

The remainder of this paper is organized as follows. The following section reviews current practice of mount characterization via the VPT. Subsequently, an enhanced VPT is proposed, accounting for fixture flexibility while maintaining six DOF per connection point. Next, this approach is validated numerically and experimentally. Finally, the main conclusions are summarized.

Dynamic mount characterization through the virtual point transformation

In the context of this work, mount characterization refers to determining the dynamic mount stiffness matrix $\mathbf{Z} \in \mathbb{R}^{12\times 12}$ for a pre-determined frequency range of interest [6]. This matrix is defined per frequency f, or pulsation $\omega = 2\pi f$, by equation 1. It describes a linear steady-state relation between the generalized force vectors $m_1, m_2 \in \mathbb{R}^{6\times 1}$ acting on both connection points and the corresponding displacement vectors $q_1, q_2 \in \mathbb{R}^{6\times 1}$. Both interfaces to adjacent components are thus represented in a lumped manner, such that a complete description requires 3 translational and 3 rotational DOF per connection point.

$$\begin{bmatrix} m_1 \\ m_2 \end{bmatrix} = \underbrace{\begin{bmatrix} \mathbf{Z_{11}} & \mathbf{Z_{12}} \\ \mathbf{Z_{21}} & \mathbf{Z_{22}} \end{bmatrix}}_{\mathbf{Z}(\omega)} \begin{bmatrix} q_1 \\ q_2 \end{bmatrix} \tag{1}$$

Besides the frequency of excitation, the mount stiffness also depends on the static preload, the temperature, and the vibration amplitude (see e.g. [7]). In general, equation 1 thus defines a linearized stiffness matrix, obtained e.g. under the static pre-load corresponding to the assembly design, for a grid of different pre-load and temperature values, etcetera.

The main diagonal blocks describe the relation between an excitation and a response on the same side (with the other side held fixed), whereas the off-diagonal blocks describe the *transfer dynamics* from one side to another. Under the assumption of conservation of force, i.e. $m_1 = -m_2$, a direct consequence is that $\mathbf{Z_{11}} = -\mathbf{Z_{21}}$ and $\mathbf{Z_{22}} = -\mathbf{Z_{12}}$. This assumption is valid below the first internal resonance of the mount. In that frequency range, it simplifies the mount characterization because only the transfer stiffness dynamics must be identified [10]. Moreover, the transfer stiffnesses ($\mathbf{Z_{21}}$ and $\mathbf{Z_{12}}$) are not affected by the eventual addition of mass, or even more complex dynamics, on either side of the mount [9, 10].

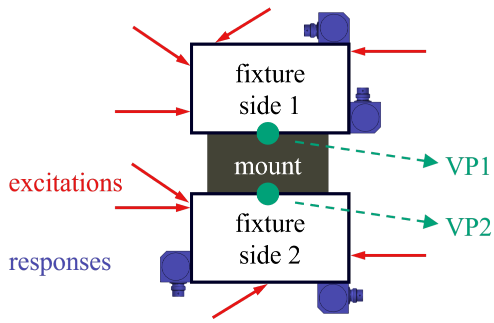

Fig. 1 Schematic of a measurement setup, with two virtual points and their associated excitation and response DOF.

Experimental methods exist to identify parts of $\mathbf{Z}$ in a direct manner, e.g. fixing $q_2 = 0$ and measuring parts of q_1, m_2 on off-the-shelf available hydraulic testing machines (see e.g. [6, 7]). Two notable diffulties arise, though. The first is the requirement to fix all DOF on one side. The second is the fact that exciting and measuring rotational DOF is problematic in practice. The first difficulty is relaxed by noting that in any assembly, such as the one of Figure 1, the characteristics of the mount itself can be determined indirectly from measured FRF data, via sub-structure decoupling or inverse substructuring techniques [10, 7]. The second difficulty is circumvented by exciting and measuring in various points and directions, cfr. Figure 1, such that all 12 DOF of the model (equation 1) are excited and measured. For each side of the mount and for both references and responses, the measured data must then be projected onto a 6-dimensional subspace corresponding to the 6 DOF of a virtual point. A widely used projection is the so-called virtual point transformation [8]. Because one VPT, linked to one virtual point, is defined per side of the mount, we use the generic subscript $k \in \{1, 2\}$ to distinguish between both sides. It is noteworthy that when not excited, and unlike the general depiction of Figure 1, both virtual points usually coincide by definition.

The original VPT assumes that all $n_u > 6$ measurement DOF behave as one rigid body, and likewise for all $n_f > 6$ excitation DOF. Under this assumption, all physically measured data on side k can be thought of as being extrapolated from six (virtual) response DOF and six (virtual) excitation DOF, cfr. equation 2.

$$u_k = \mathbf{R}_{u,k} q_k, \qquad m_k = \mathbf{R}_{f,k}^T f_k, \qquad k \in \{1, 2\} \tag{2}$$

In the matrices $\mathbf{R}_u \in \mathbb{R}^{n_u \times 6}$ and $\mathbf{R}_f \in \mathbb{R}^{n_f \times 6}$, each column corresponds to a rigid-body mode. These matrices are constructed from geometric information, namely the positions and orientations of the evaluated DOF with respect to the virtual point. Their pseudo-inverses, denoted with $\cdot^\dagger$, form the projection matrices $\mathbf{T}_u$ and $\mathbf{T}_f^T$. Those projections are applied respectively on the responses (u) and references (forces f), as in equation 3.

$$q_k = \mathbf{R}_{u,k}^\dagger u_k \triangleq \mathbf{T}_{u,k} u_k, \qquad f_k = \left(\mathbf{R}_{f,k}^T\right)^\dagger m_k \triangleq \mathbf{T}_{f,k}^T m_k \tag{3}$$

By applying the VPT to the FRF data as in equation 4, one obtains the projected FRF matrix $\mathbf{H}_{qm} \in \mathbb{R}^{12\times 12}$. By inverting the latter, one may readily obtain the coupled assembly's stiffness matrix $\mathbf{Z^C}$ [10]. Assuming acceleration-level responses, this is made explicit in equation 5. The off-diagonal blocks in $\mathbf{Z^C}$ already describe the transfer dynamics of the mount itself, i.e. $\mathbf{Z_{12}^C} = \mathbf{Z_{12}}$ and $\mathbf{Z_{21}^C} = \mathbf{Z_{21}}$. One may derive $\mathbf{Z_{11}}$ and $\mathbf{Z_{22}}$ from $\mathbf{Z^C}$ via substructure decoupling or inverse substructuring [10].

$$\mathbf{H}_{qm} = \begin{bmatrix} \mathbf{H_{11}} & \mathbf{H_{12}} \\ \mathbf{H_{21}} & \mathbf{H_{22}} \end{bmatrix} = \mathbf{T}_u \mathbf{H}_{uf} \mathbf{T}_f^T = \begin{bmatrix} \mathbf{T}_{u,1} & \mathbf{0} \\ \mathbf{0} & \mathbf{T}_{u,2} \end{bmatrix} \begin{bmatrix} \mathbf{H}_{u_1 f_1} & \mathbf{H}_{u_1 f_2} \\ \mathbf{H}_{u_2 f_1} & \mathbf{H}_{u_2 f_2} \end{bmatrix} \begin{bmatrix} \mathbf{T}_{f,1} & \mathbf{0} \\ \mathbf{0} & \mathbf{T}_{f,2} \end{bmatrix}^T \tag{4}$$

$$\mathbf{Z^C}(\omega) = \begin{bmatrix} \mathbf{Z_{11}^C} & \mathbf{Z_{12}^C} \\ \mathbf{Z_{21}^C} & \mathbf{Z_{22}^C} \end{bmatrix} = \begin{bmatrix} \mathbf{Z_{11}^C} & \mathbf{Z_{12}} \\ \mathbf{Z_{21}} & \mathbf{Z_{22}^C} \end{bmatrix} = -\omega^2 \mathbf{H}_{qm}^{-1} = -\omega^2 \begin{bmatrix} \mathbf{H_{11}} & \mathbf{H_{12}} \\ \mathbf{H_{21}} & \mathbf{H_{22}} \end{bmatrix}^{-1} \tag{5}$$

Any error resulting from the VPT (equation 4) is detrimental to the accuracy of the dynamic stiffness characteristics obtained through equation 5. This limits the maximum frequency of identification, because of the assumption that the (instrumented and excited) fixtures behave rigidly. Typically, one verifies this assumption using the so-called *sensor consistency* metric ρ_u^2 and *impact consistency* metric ρ_f^2 [8]. In equation 6, H_{f_h} denotes a column of $\mathbf{H}$ that corresponds to a distant excitation DOF f_h and H_{u_i} denotes one row, corresponding to the i-th response DOF. In equation 7, the superscript $\cdot^H$

denotes the Hermitian transpose.

$$\rho_u^2(f_h) \triangleq \text{MAC}\left(\mathbf{R}_u \mathbf{T}_u H_{f_h}, H_{f_h}\right), \qquad \rho_f^2(u_i) \triangleq \text{MAC}\left(\mathbf{R}_f \mathbf{T}_f H_{u_i}, H_{u_i}\right) \tag{6}$$

$$\text{MAC}(a,b) \triangleq \frac{\left(a^H b\right)\left(b^H a\right)}{\left(a^H a\right)\left(b^H b\right)}, \quad a,b \in \mathbb{R}^{n\times 1} \tag{7}$$

In this work, we define the average sensor consistency of a VPT to be the sensor consistency (as function of frequency) averaged over all excitations linked to it. *Vice versa*, the average impact consistency of a VPT is the average over all sensors linked to it.

Enhanced Virtual Point Transformation to Account for Fixture Flexibility

To extend the validity of the VPT towards frequencies near the first eigenfrequency of a fixture, one must add flexible modes to $\mathbf{R}_u$ and $\mathbf{R}_f$. In the context of DS, an ad-hoc selection from a library of flexible modes has been proposed to this end [11]. This works well if one can accurately predict the deformation in the vicinity of the virtual point from engineering insight. Alternatively, a polynomial fit onto the measured flexible deformation may be applied. In general, this leads to an overly large amount of extra DOF η, being the participation factors to the flexible modes. The allowed strain fields are therefore constrained to those of e.g. an idealized beam or thin plate [12]. Again, one must choose which constraint to apply based on engineering insight. In this case, one cannot add any amount of extra DOF η, because e.g. assuming plate-like behavior yields two bending modes and one torsion mode, and hence 3 additional DOF.

Besides the choice of deformation mode shapes, the introduction of flexible modes to the VPT causes another major difficulty in the context of virtual prototyping. Namely, to enforce compatibility between two components requires that the mode shapes on both components are matched. In other words, it is not sufficient to decide on a common number of flexible modes. This requirement is not straightforward to fulfill, because different component models may originate from different teams or vendors. For rubber mount models, however, a subsequent projection onto 6 DOF per side may be applied, as explained in the following.

Firstly, we propose that the extension to the VPT be based on eigenmodes of the fixtures. This is an attractive choice because (i) the fixtures used for mount identification are usually easy to model, (ii) the first few eigenmodes of the fixture are not expected to be overly affected by the presence of a rubber mount, and they are insensitive to e.g. a wrongly assumed material density or Young's modulus, and (iii) the problem of selecting which modes to include is trivial; one should just add one or multiple eigenmodes in order of increasing eigenfrequency. Secondly, we propose that the addition of extra (flexible) DOF merely be used to improve the consistency between measured (physical) and generalized (lumped, virtual) responses or excitations. In other words, we aim to consider the effect of the fixtures' deformation on the 6 DOF on each side of the mount model, without adding flexible DOF to the mount model. This approach is justified as long as the local interface between fixture and mount does not deform significantly in the first few eigenmodes of the fixtures, or as long as any such local deformation on one side of the mount does not cause energy to transfer through the mount.

In the following, the FE-based eigenmodes are assumed to be partitioned as in equation 8, where the subscripts indicate the required selection of DOF. One may note the requirement to evaluate the mode shape vectors in the DOF associated to the virtual point. This partition $\phi_q \left(= \phi_m\right) \in \mathbb{R}^{6\times n_\eta}$ is generally not available from test data, for the same reasons that motivate the use of the VPT. One may straightforwardly extract them from a FEM, though.

$$\phi_k^T \triangleq \begin{bmatrix}\phi_{u,k}^T & \phi_{f,k}^T & \phi_{q,k}^T\end{bmatrix}, \qquad k \in \{1,2\} \tag{8}$$

Through concatenating $\mathbf{R}_u$ and $\mathbf{R}_f$ with the corresponding partitions of the n_η flexible modes, as in equation 9, the extended VPT is defined as in equation 10. Its application will require the extended projection matrices $\mathbf{T}^*$, obtained via equation 11. In these equations, the modal participation factors ρ and η correspond to the rigid and flexible modes, respectively, and g_ρ and g_η denote the associated generalized forces.

$$\mathbf{R}_{u,k}^* \triangleq \begin{bmatrix}\mathbf{R}_{u,k} & \phi_{u,k}\end{bmatrix} \qquad \mathbf{R}_{f,k}^* \triangleq \begin{bmatrix}\mathbf{R}_{f,k} & \phi_{f,k}\end{bmatrix} \tag{9}$$

$$u_k = \mathbf{R}_{u,k}^* \begin{bmatrix}\rho_k \\ \eta_k\end{bmatrix}, \qquad \begin{bmatrix}g_{\rho,k} \\ g_{\eta,k}\end{bmatrix} = \left(\mathbf{R}_{f,k}^*\right)^T f_k \tag{10}$$

$$\begin{bmatrix}\rho_k \\ \eta_k\end{bmatrix} = \left(\mathbf{R}_{u,k}^*\right)^\dagger u_k \triangleq \mathbf{T}_{u,k}^* u_k, \qquad f_k = \left(\left(\mathbf{R}_{u,k}^*\right)^T\right)^\dagger \begin{bmatrix}g_{\rho,k} \\ g_{\eta,k}\end{bmatrix} \triangleq \left(\mathbf{T}_{f,k}^*\right)^T \begin{bmatrix}g_{\rho,k} \\ g_{\eta,k}\end{bmatrix} \tag{11}$$

A mere substitution of the projection matrices $\mathbf{T}$ with $\mathbf{T}^*$ in equation 4 would not yield the desired FRF matrix $\mathbf{H}_{qm} \in \mathbb{R}^{12\times 12}$. Instead, the projected FRF matrix would contain $12 + n_\eta$ rows and columns, due to the additional flexible DOF. Aiming to preserve only 6 DOF per virtual point, the flexible contribution to the response vector $q \in \mathbb{R}^{6\times 1}$ is evaluated at the virtual point and added to the rigid contribution ρ, cfr. equation 12. Regarding the excitation, equation 12 states that the excitation vector $m \in \mathbb{R}^{6\times 1}$, while acting on the virtual point, excites both rigid and flexible modes of the fixture. In relation to the measured FRF matrix, this addition boils down to a subsequent projection that maps the contribution of the (measured and excited) flexible modes onto the preserved 6 DOF of each virtual point, as in equation 13.

$$q_k = \rho_k + \phi_{q,k}\eta_k, \qquad \begin{bmatrix} g_{\rho,k} \\ g_{\eta,k} \end{bmatrix} = \begin{bmatrix} m_k \\ \phi_{q,k}^T m_k \end{bmatrix} \tag{12}$$

$$\mathbf{H}^*_{qm} = \begin{bmatrix} \mathbf{I} & \phi_{q,1} & \mathbf{0} & 0 \\ \mathbf{0} & 0 & \mathbf{I} & \phi_{q,2} \end{bmatrix} \mathbf{T}^*_u \mathbf{H}_{uf} \left(\mathbf{T}^*_f\right)^T \begin{bmatrix} \mathbf{I} & \phi_{q,1} & \mathbf{0} & 0 \\ \mathbf{0} & 0 & \mathbf{I} & \phi_{q,2} \end{bmatrix}^T \tag{13}$$

The here obtained FRF matrix $\mathbf{H}^*_{qm}$ describes how the excitations m_k and (displacement-level) responses q_k, *as introduced in equation 1*, relate to one another in the test assembly. It is thus fully equivalent to H_{qm} as obtained through equation 4. Equation 5 thus remains valid, i.e. one must merely substitute $\mathbf{H}_{qm}$ with $\mathbf{H}^*_{qm}$ to obtain the transfer dynamics of the mount itself. In conclusion, the proposed variant to the VPT is not an extended VPT, in the sense that the projected dynamics are captured using 6 DOF on each side of the interface, like is the case for the original VPT. It is enhanced, because in contrast to the original VPT, the flexibility of the fixtures is taken into account.

Finally, one may remark – from the block-diagonal structure of all projection matrices in equation 13 – that the amount of flexible DOF n_η may differ from side to side. One may thus apply the here proposed approach on side 1 and the original VPT on side 2. To maintain the generally recommended over-determination factor of 2, one should add two response channels and two excitations per flexible DOF considered. Similarly to the original VPT, the instrumentation and excitation layout can be checked based on the condition numbers of the matrices $\mathbf{R}^*$.

The following section presents a numerical validation, highlighting the benefits of extending the reduction basis with flexible eigenmodes. The experimental validation of the subsequent section demonstrates the added value of the enhanced VPT, which includes the second projection onto 6 DOF, for dynamic mount stiffness identification.

Numerical Validation of the Enhanced VPT

Figure 2 illustrates the numerical validation setup. It represents a 30 mm thick plate, modeled using linear hexahedral elements of size 5 mm. This 3D model was used previously for validating a polynomial fitting approach, assuming an idealized thin-plate strain field. The here presented validation includes a comparison against that polynomial fitting approach [12]. We consider only the projection of $8 \times 3 = 24$ response DOF (u_1) onto the 6 DOF (q_1) of 1 virtual point, for a single excitation DOF f_h, cfr. equation 14. For this single-sided projection, equation 13 simplifies into 14. This simplification does not affect the validation, because dealing with a perfectly reciprocal model, one may interchange the notions of response DOF and reference DOF.

$$\mathbf{H}^*_{q_1 f_h} = \begin{bmatrix} \mathbf{I} & \phi_{q,1} \end{bmatrix} \mathbf{T}^*_{u,1} \mathbf{H}_{u_1 f_h} = \begin{bmatrix} \mathbf{I} & \phi_{q,1} \end{bmatrix} \begin{bmatrix} \mathbf{R}_{u,1} & \phi_{u,1} \end{bmatrix}^{\dagger} \mathbf{H}_{u_1 f_h} = \begin{bmatrix} \mathbf{I} & \phi_{q,1} \end{bmatrix} \begin{bmatrix} \mathbf{H}_{\rho_1 f_h} \\ \mathbf{H}_{\eta_1 f_h} \end{bmatrix} \tag{14}$$

The focus of this numerical validation is on the choice of extending $\mathbf{R}_u$ with flexible eigenmodes ϕ_u. Figure 3 shows that with only a single extra DOF, being the participation factor to one flexible eigenmode, a significantly higher sensor consistency is obtained than with three extra DOF in the case of the polynomial plate model fit. It must be noted that in this case, the single extra DOF is chosen to correspond to the second bending mode. This choice is made because, as one can see in Figure 2, the selected responses are located such that the first bending mode introduces little deformation. Even so, the benefits of using flexible eigenmodes are clear: with an equal amount of flexible DOF ($n_\eta = 3$), the reduction basis extended with eigenmodes clearly outperforms the one based on the polynomial plate model. Using m perfectly identified mode shapes, the consistency is virtually perfect up to the m-th eigenfrequency. Noting that in Figure 3, eigenfrequencies f_1 to f_{12} are marked by vertical lines, this is illustrated also for $m = 12$. In case of closely spaced modes (around 900 Hz), this holds approximately.

Another significant benefit in practical applications, is the fact that one can freely select the amount of relevant DOF to consider. In Figure 3, for example, it is clear that by accounting for only two bending modes ($n_\eta = 2$), one can already capture very accurately the local flexibility observed in the region of indicator points up to about 1500 Hz. In this case,

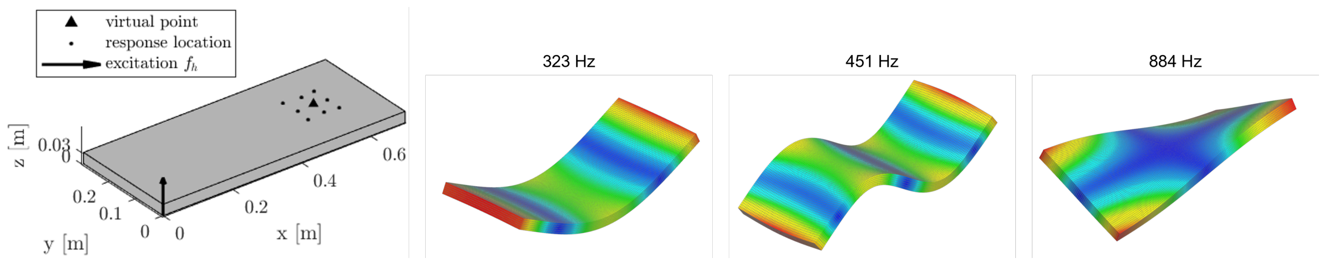

Fig. 2 Numerical validation setup, and first three flexible eigenmodes.

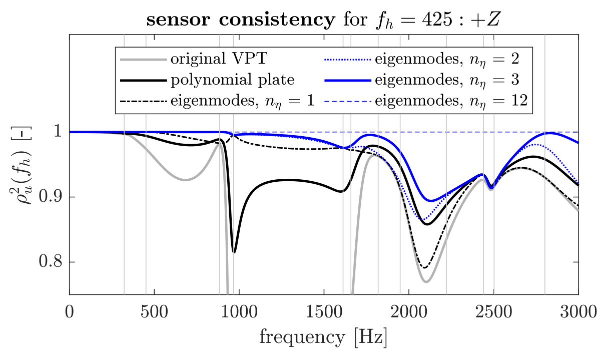

Fig. 3 Sensor consistency obtained with different reductions onto $6 + n_\eta$ response DOF.

adding the third extra DOF would either add to the required instrumentation effort, or reduce the level of over-determination. One such disadvantage would be unavoidable in case of the polynomial plate model.

Using FE based modeshapes also has advantages over a generic library of shapes [11]. Firstly, the here proposed FE based approach is targeted towards the specific fixtures by definition. The corresponding shapes may thus be expected to yield better consistencies than the generic shapes, or allow to obtain similar consistencies with fewer extra DOF. Secondly, an FE based approach allows to synthesize consistency curves like those of Figure 3 prior to the test campaign. These can guide one to select required mode shapes, as well as the appropriate amount, locations and orientations of sensors (and excitations).

Experimental Validation: High-Frequency Dynamic Mount Stiffness Identification

Figure 4 shows the experimental validation setup. Its intent is to characterize an automotive rubber mount, of which the inner core (side 1) is connected to a vehicle body and the outer cylinder (side 2) to a powertrain subframe. Figure 4a also shows the two cross-shaped fixtures on side 1 and one square-shaped fixture on side 2. The expected result is the 12-by-12 matrix of mount stiffness curves of equation 1, with both virtual points (denoted as VP1 and VP2) located at the center of the mount.

As visible in Figure 4b, side 1 is instrumented with two tri-axial accelerometers on each cross, hence 12 response DOF are measured on this side. An impact hammer has been used for the excitation; 9 DOF were excited on side 1. On side 2, 11 DOF are excited, and 12 response DOF are measured using four tri-axial accelerometers. This amounts to 432 FRF, acquired from 0 Hz to 3.2 kHz with a 1 Hz resolution. Based on their input-output coherences, the useful bandwidth reaches up to 2.5 kHz. Within this bandwidth, measured operational deflection shapes on side 1 reveal a torsion mode at about 1.77 kHz and two bending modes at 2.19 kHz and 2.47 kHz, respectively. As will be shown below, these flexibilities cause the average sensor and impact consistencies of the original VPT to fall below 0.8 at 1.3 kHz. On side 2, the average sensor and impact consistencies of the original VPT fall below 0.8 and 0.9, respectively, at the frequency of 2 kHz.

Following the above, the enhanced VPT is applied on side 1 of the mount, while the original VPT is applied on side 2. As such, the frequency range of mount stiffness identification can potentially be extended from 1.3 kHz to 2 kHz. Figure 4c shows the therefore constructed FEM of side 1. Although the case at hand is an assembly, the FEM is obtained straightforwardly. It consists of linear tetrahedral elements, does not include the threaded rod, washers and nuts holding the real assembly together, and it was not updated in any way. From it, modal displacements are extracted in the sensor and impact

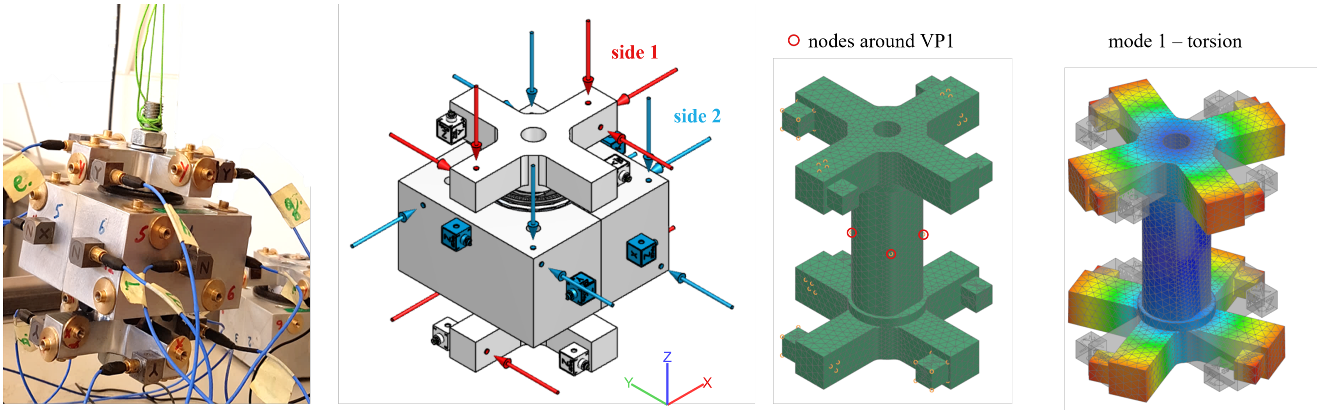

(a) (b) (c) (d)

Fig. 4 Experimental setup (a) with geometry definition (b), and FEM of side 1 (c) with flexible eigenmode prediction (d).

locations, cfr. equation 9, and modal displacements and rotations in VP1 (equation 13) are obtained from 4 nodes nearby the center of the mount. Figure 4d shows the first predicted flexible (torsion) eigenmode. The subsequent two eigenmodes are bending modes.

Figure 5 shows the effect of extending the VPT, as in equation 11, with $n_\eta \in \{1, 2, 3\}$ flexible eigenmodes on the averaged sensor and impact consistencies. In these graphs, the vertical lines indicate the approximate eigenfrequencies as obtained from analyzing the operational deflection shapes. Between 1.3 kHz and 2 kHz, a significant improvement is observed even when considering only one flexible (torsion) eigenmode. As expected, the consistency further increases when introducing more than one flexible DOF. For the given dataset, however, doing so would lead to very low levels of over-determination for the inversions required in equation 11[1]. Because of this, combined with the lower data quality above 2 kHz, only the torsion mode is considered in the remainder of this preliminary experimental validation.

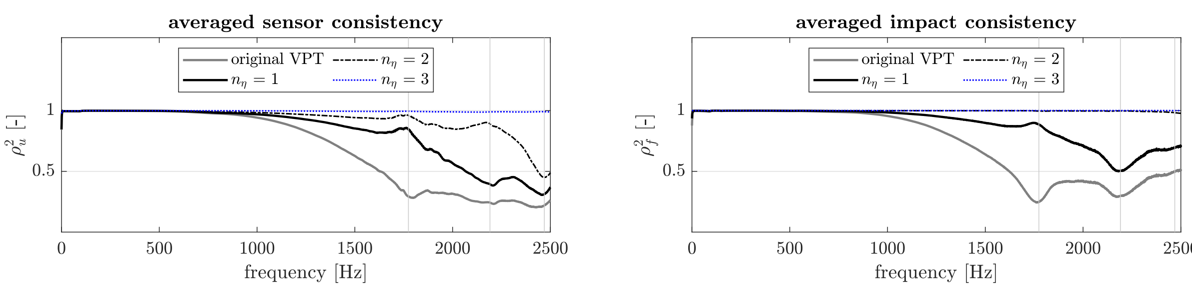

Fig. 5 Sensor consistency (left) and impact consistency (right) obtained on side 1, with different reductions onto 6+n_η DOF.

Figure 6 shows a selection of FRF obtained from, respectively, the original VPT (equation 4) and the enhanced VPT (equation 13). The enhanced VPT does not suffer from the spurious effect that the first torsion mode has on the results of the original VPT. This is indeed an improvement, because exciting the side 1 assembly in the considered DOF of VP1 should not excite the first torsion mode. As expected, the effect of bending behavior still affects the driving point FRF, notably in the '+X' direction. Figure 7 shows the corresponding selection of transfer FRF. Unlike the FRF of Figure 6, these transfer FRF have remained invariant to the enhancement of the VPT. This may indicate that excitation of the considered torsion mode does not lead to energy transfer through the mount, as such validating the approach of projecting $6 + n_\eta$ DOF onto 6 DOF.

Finally, Figure 8 compares the enhanced VPT to the original VPT in terms of mount transfer stiffness curves. The latter are derived from the 12-by-12 matrix of projected FRF as per equation 5. Above 1.75 kHz onwards, these results are still affected by the presence of bending. However, the enhanced VPT avoids the significant excursions from the expected (smooth and flat) mount stiffness curves up to this frequency, whereas the original VPT leads to problematic deviations already from 1.3 kHz onwards. Thus, by accounting for the first torsion mode, the proposed approach has extended the

The perfect impact consistency for $n_\eta = 3$ is even a trivial result, because the projection onto $6 + 3 = 9$ excitation DOF is not a reduction in this case.

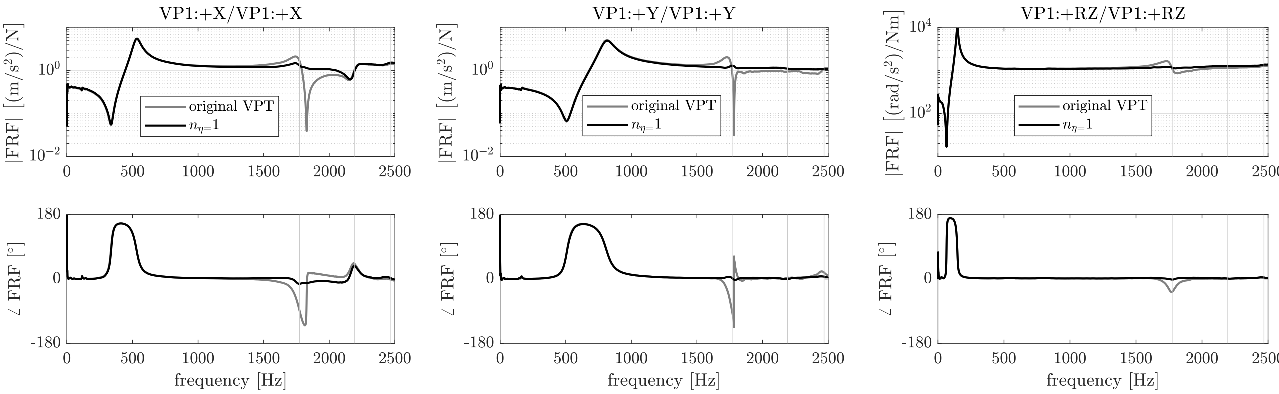

Fig. 6 Direct FRF resulting from either the original VPT, or the proposed approach using $n_\eta = 1$ flexible torsion mode.

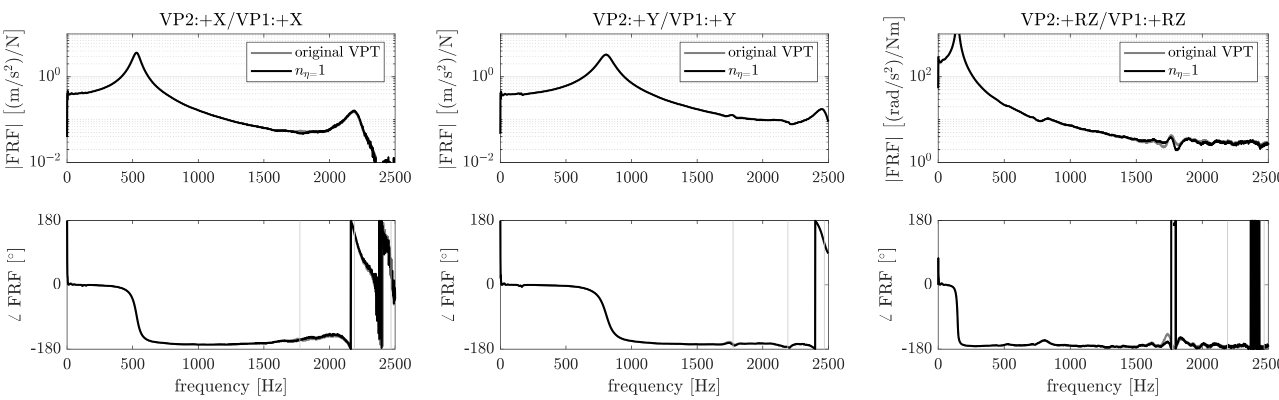

Fig. 7 Transfer FRF resulting from either the original VPT, or the proposed approach using $n_\eta = 1$ flexible torsion mode.

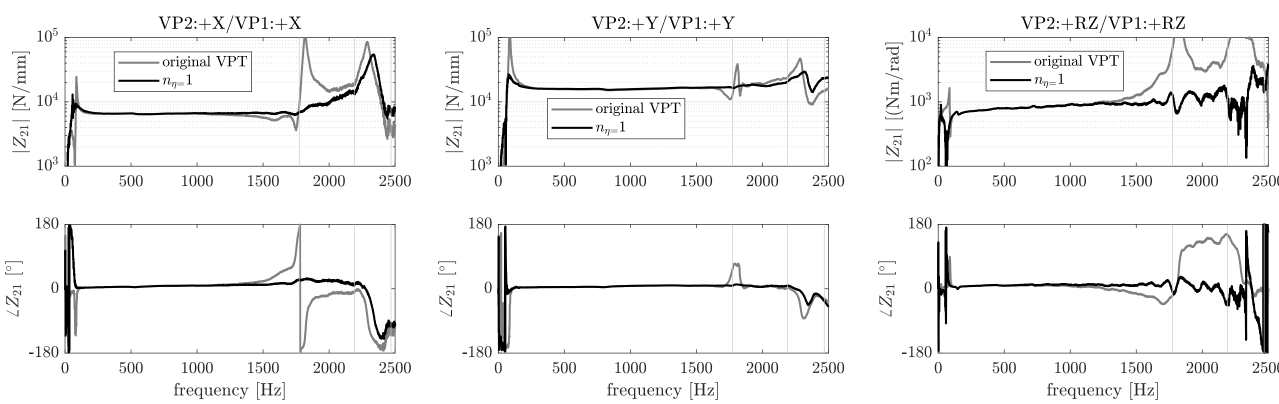

Fig. 8 Transfer stiffness curves that result from either the original VPT, or the proposed approach with $n_\eta = 1$.

useful bandwidth for mount characterization by about 450 Hz (34 %). This result is promising, considering that the FEM based nature of the proposed enhancement is well suited for optimizing instrumentation and/or fixture designs employed in future test campaigns.

Conclusion

This work has targeted the indirect identification of mount stiffness characteristics from FRF measurements over an extended frequency bandwidth. To achieve this, an enhancement to the virtual point transformation (VPT) has been proposed and validated. It accounts for flexibility of the fixtures, which violates the original VPT's primary assumption of rigidity. The proposed enhancement is based on two novelties, namely (i) the use of finite element model based eigenmodes for enriching the basis of the VPT's reduction space, and (ii) an additional reduction onto the six DOF associated to the virtual point. The latter reduction is critical in order to obtain a mount model which can be readily applied in virtual prototype assemblies. A numerical validation has highlighted the value of extending the reduction basis with eigenmodes, in terms of the consistency improvement per additional DOF to identify. A preliminary experimental validation of the proposed approach has shown that, by accounting for the first torsion mode of the fixture assembly at hand, the enhanced VPT is valid over a +30 % larger bandwidth than the original VPT. As such, the proposed approach has allowed to extend the validity of the identified 12-by-12 stiffness matrix, to beyond the first eigenfrequency introduced by the fixture assembly. Future work will consider the identification of multiple flexible DOF already in the test setup definition, aiming to demonstrate the full potential of the here proposed enhanced VPT.

Acknowledgments This research was partially supported by VLAIO (Flanders Innovation & Entrepreneurship Agency) within the O&O project ADRENALINE (Advanced modular approaches for cabin noise analysis in EVs), VLAIO O&O project no. 2022.1027.

References

1. Moorhouse, A., Elliott, A., and Meggitt, J. "Virtual acoustic prototyping - a story of four decades". In *Proceedings of Inter-noise 2023*, Glasgow, Scotland (2022).
2. Bianciardi, F., Salamone, N., Colangeli, C., Ortega Almirón, J., Verrecas, B., Corbeels, P., and Janssens, K. "NVH prediction and real-time auralization for virtually assembled vehicles: An overview of the technology". In *Proc. SAE Noise and Vibration Conference and Exhibition*, MI, United States (2023).
3. van der Seijs, M., de Klerk, D., and Rixen, D. "General framework for transfer path analysis: History, theory and classification of techniques". *Mechanical Systems and Signal Processing*, 68-69:217–244 (2016).
4. Jetmundsen, B., Bielawa, R.L., and Flannelly, W.G. "Generalized frequency domain substructure synthesis". *Journal of the American Helicopter Society*, 33(1):55–64 (1988).
5. de Klerk, D., Rixen, D.J., and Voormeeren, S.N. "General framework for dynamic substructuring: History, review and classification of techniques". *AIAA Journal*, 46(5):1169–1181 (2008).
6. International Organization for Standardization. *DIN EN ISO 10846-1:2008 Acoustics and vibration — Laboratory measurement of vibroacoustic transfer properties of resilient elements – Part 1: Principles and guidelines*. ISO (2008).
7. Haeussler, M., Klaassen, S., and Rixen, D. "Experimental twelve degree of freedom rubber isolator models for use in substructuring assemblies". *Journal of Sound and Vibration*, 474:115253 (2020).
8. van der Seijs, M.V., van den Bosch, D.D., Rixen, D.J., and de Klerk, D. "An improved methodology for the virtual point transformation of measured frequency response functions in dynamic substructuring". In *4th ECCOMAS thematic conference on computational methods in structural dynamics and earthquake engineering*, volume 4 (2013).
9. Meggitt, J.W.R., Elliott, A.S., Moorhouse, A.T., and Lai, H.K. "In situ determination of dynamic stiffness for resilient elements". *Proceedings of the institution of mechanical engineers, Part C: Journal of mechanical engineering science*, 230(6):986–993 (2016).
10. Meggitt, J. and Moorhouse, A. "In-situ sub-structure decoupling of resiliently coupled assemblies". *Mechanical Systems and Signal Processing*, 117:723–737 (2019).
11. Pasma, E., van der Seijs, M.V., Klaassen, S., and van der Kooij, M. "Frequency based substructuring with the virtual point transformation, flexible interface modes and a transmission simulator". In *Dynamics of Coupled Structures: Proceedings of the 36th IMAC, A Conference and Exposition on Structural Dynamics*, volume 4, pages 205–213. Springer (2018).
12. Ortega Almirón, J., Bianciardi, F., and Desmet, W. "Flexible interface models for force/displacement field reconstruction applications". *Journal of Sound and Vibration*, 534:117001 (2022)